Journal of Quantitative Spectroscopy & Radiative Transfer 338 (2025) 109412

Contents lists available at ScienceDirect

Journal of Quantitative Spectroscopy and Radiative Transfer

journal homepage: www.elsevier.com/locate/jqsrt

An accurate determination of O_2 A-band line intensities through experiment and theory

Erin M. Adkins [a,*], Sergei N. Yurchenko [b], Wilfrid Somogyi [b], Joseph T. Hodges [a]

[a] Chemical Sciences Division, National Institute of Standards and Technology, 100 Bureau Drive, Gaithersburg, MD 20899, USA
[b] Department of Physics and Astronomy, University College London, Gower Street, London WC1E 6BT, United Kingdom

ARTICLE INFO

Dataset link: https://data.nist.gov/

Keywords:
Oxygen
Line intensities
Cavity ring-down spectroscopy

ABSTRACT

Accurate intensities of the O_2 A-band $\left[b^1\Sigma_g^+ \leftarrow X^3\Sigma_g^-(0,0)\right]$ centered about 760 nm are essential to reduce biases in satellite- and ground-based remote measurements of column-integrated air mass and greenhouse gas concentration. In support of these remote sensing techniques, we made cavity ring-down spectroscopy measurements of $^{16}O_2$ A-band line intensities up to $J = 40$, and we extrapolated these values to $J = 60$ using scaled *ab initio* intensity calculations. The J dependences of the measured and theoretical intensities differ on average by less than 0.1 %, and the measured intensities have relative combined standard uncertainties at the 0.15 % level. Upon evaluation of the integrated intensity, we find a negative bias between literature results and this work, which is four times greater than our present uncertainty.

1. Introduction

The determination of airmass plays a key role in satellite- and ground-based remote sensing measurements of greenhouse gases (GHGs) relying on the absorption of solar radiation through an atmospheric column. To this end, the measurement of light absorption by atmospheric O_2 can readily provide column-integrated airmass because it has a well-known, stable, and uniform mole fraction in the atmosphere. O_2 is also used in remote sensing measurements for the determination of temperature profiles [1–5], aerosol [1,6] and cloud [7,8] properties. For observations in the near-infrared region, the O_2 A-band $\left[b^1\Sigma_g^+ \leftarrow X^3\Sigma_g^-(0,0)\right]$ is the strongest and most often used absorption band for satellite measurements. This band is used in the GOSAT (Greenhouse Gases Observing Satellite) [9], SCIAMACHY (scanning imaging absorption spectrometer for atmospheric cartography) [10], TROPOMI (Tropospheric Monitoring Instrument) [11], and OCO-2/3 (Orbiting Carbon Observatory) [12,13] missions for measuring airmass.

The OCO missions have a target dry air carbon dioxide (CO_2) mole fraction precision of 1 mmol mol^{-1} (0.25 % of 425 mmol mol^{-1}) to provide the precision and resolution to quantify regional CO_2 sources and sinks [13–15]. Spectroscopic uncertainty is a key source of bias in the retrievals, and physically consistent spectroscopic models are critical to achieving the desired accuracy targets [16,17]. The O_2 A-band absorption cross sections used by OCO are generated from an integrated self-consistent line-by-line spectroscopic model involving advanced line shapes, line mixing, and broadband collision-induced absorption (CIA) [18,19]. The most recent O_2 spectroscopic updates resulted in a flattening of the latitudinal surface pressure bias [18] compared to the previous update [19]. However, a global surface pressure bias and structured spectral residuals in the retrievals remain [18]. These discrepancies indicate that there is still potential for improvement in the O_2 A-band spectroscopic model that could minimize spectroscopy-related biases in atmospheric retrievals.

Spectroscopic uncertainty in the O_2 A-band has long been ascribed to the uncertainties in and correlations between the measured line mixing and CIA components [17,19,20]. However, accurate determinations of these higher-order components of the spectroscopic model require line intensities with low uncertainties.

Several previous works have thoroughly summarized the history of O_2 A-band line intensity measurements [21–23]. Here, we will focus on studies reporting band-wide transition resolved intensity measurements with band intensities within the literature consensus region, which is nominally centered at 2.25×10^{-25} cm molecule^{-1} with a width that is $\pm$ 2 % of this value [18,19,21–30].

Ritter and Wilkerson measured 54 transitions across the O_2 A-band using a tunable dye laser (TDL) and a White cell at pressures between 10 kPa and 100 kPa of pure O_2. These spectra were fit individually with a

---

* Corresponding author.
E-mail address: erin.adkins@nist.gov (E.M. Adkins).

https://doi.org/10.1016/j.jqsrt.2025.109412
Received 10 January 2025; Received in revised form 26 February 2025; Accepted 26 February 2025

Galatry profile [24]. To model the measured intensities, they included a transition-dependent factor that captures the non-Boltzmann, rotational dependence of the intensities, and the coupling of the electron spin to the molecular axis of the ground state. They investigated several different expressions for modeling the rotational line intensities, concluding that the model for calculating the Hönl-London (HL) factors proposed by Watson [31], which we refer to as the Watson model (described below) agreed with their observations to within their measurement uncertainty [24].

Several Fourier transform spectroscopy (FTS) measurements from different institutions published across several decades reported transition-resolved intensities within the consensus region. Schermaul and Learner studied transitions up to $J = 33$ in pure O_2 at pressures between 2.1 kPa and 100 kPa at 198 K and 296 K. The measured intensities were determined through single spectrum fits with a Voigt profile with modified Doppler widths to account for collisional (Dicke) narrowing [25]. Brown and Plymate reported line intensities for transitions up to $J = 22$ from FTS measurements at temperatures between 202 K and 296 K, pressures between 20 kPa to 80 kPa, and with pure O_2 where the transitions were fit with a Voigt profile single spectrum [21]. Predoi-Cross et al. measured line intensities up to $J = 55$ at 296 K for pure O_2 samples at pressures between 1 kPa and 400 kPa and used multispectrum fitting with Voigt, speed-dependent Voigt (SDV), and Galatry profiles with line-mixing [23]. Schermaul and Learner modeled the rotational dependence of the intensities also using the Hönl-London factors reported by Watson [31]. They observed a linear deviation between experiment and theory in the total angular quantum number dependence of the intensity. They attributed this discrepancy to rotation-vibration interactions which are not included in the Watson model [25], although Brown and Plymate were not able to confirm this effect [21]. Using the Watson model, Predoi-Cross et al. also reported a linear discrepancy between the measured and modeled rotational dependence of the intensities [23]. Most recently, Petrova et al. reported line intensities up to $J = 20$ in an FTS study of carbon dioxide broadening in the O_2 A-band, which was conducted near room temperature at pressures between 6 kPa and 70 kPa and analyzed using the Voigt and SDV line shapes with multi-spectrum constraints [32].

O_2 A-band intensities in the main portion of the P-branch [22], as well as higher J transitions up to $J = 47$ in the same branch [29] and up to $J = 43$ in the R-branch [30] were measured in a series of frequency-stabilized cavity ring-down spectroscopy (FS-CRDS) experiments. All measurements were made using the same spectrometer located at the National Institute of Standards and Technology (NIST) in Gaithersburg, Maryland. These experiments were done at room temperature, for 2 % O_2 in N_2, air, and pure O_2 samples, and at pressures between 0.2 kPa and 101 kPa, where the combination of sample and pressure was adjusted on a line-by-line basis to optimize the spectrum signal-to-noise ratio. Galatry line profiles were fit to individual single-line spectra. Long et al. [30] combined these three FS-CRDS data sets [22,29,30] and observed percent level differences between the measured and fitted (Watson model) rotational dependence of the intensities. This deviation between experiment and theory was fit using a Herman-Wallis- [33] modified Watson (HWW) model, and the fitted results were included in the HITRAN 2012 O_2 A-band line intensity update [34]. Importantly, it is worth noting that the Herman-Wallis (HW) modification, which was derived to treat vibration-rotation perturbation, only empirically accounts for deviations from the Watson model because the O_2 A-band comprises vibrationless rotational-electronic transitions that exhibit effects such as spin uncoupling, orbit-rotation interaction, and spin-orbit perturbation [35].

To support spectroscopic data requirements for the NASA OCO missions, Drouin and colleagues on the NASA OCO Science Team reported a multi-spectrum analysis of laboratory data in which FTS [19] spectra acquired at Jet Propulsion Laboratory (JPL) and the FS-CRDS P-branch spectra that contributed to the Long et al. [22,30] work were combined and fit with a self-consistent spectroscopic model. This analysis incorporated the HWW intensity model, SDV profile, full-matrix first-order line-mixing effects, and CIA, thus providing line-by-line parameters suitable for forward modeling spectral cross sections. Not surprisingly, Drouin et al. [19] noted good agreement with the relative line intensities in HITRAN 2012 [36] for J less than 35, given that both studies involved the P-branch data reported in Ref. [22]. Because they found that adjustment of the HW parameters degraded the extrapolated line intensities, the HW terms were fixed to the values reported in Long et al. [30]. Their reported 0.5 % increase in the band intensity from that given by Long et al. [30] was ascribed to the inclusion of line mixing and CIA. The resulting $^{16}O_2$ A-band line intensities were archived in HITRAN 2016 [37]. Furthermore, the broadband CIA spectrum reported in Drouin et al. [19] was retrieved from solar TCCON spectra and found to differ substantially in shape from that predicted by theory [38]. Because the CIA is determined from excess spectral features after accounting for absorption by monomer lines and line mixing, this discrepancy is potential evidence of errors or uncertainties in the spectroscopic model underpinned by the O_2 A-band intensities.

The next self-consistent spectroscopic model of the O_2 A-band with line mixing and CIA reported by the OCO Science Team as reported by Payne et al. [18], incorporated additional FS-CRDS spectra collected at a range of atmospherically relevant pressures and temperatures and additional high-pressure FTS spectra. Including these additional data highlighted discrepancies in the high J intensity and line-mixing models and pointed out a symmetric J dependent inconsistency between the FTS and FS-CRDS P-branch line intensities reported in Ref. [19]. Updating the HWW intensity model to be informed by both the FTS and FS-CRDS P-branch line intensities from [19] decreased the band intensity by 1.1 % and significantly changed the HW corrections, resulting in a nominal 4 % decrease in the intensities for the highest reported J lines ($J = 45$). These revised line intensities were subsequently included in the HITRAN 2020 O_2 A-band line intensity update [39].

While the line intensity studies reported by various groups using TDL [24], FS-CRDS [22,29,30], and FTS [18,19,21,23,25,32] have reported band intensities agreeing at the ± 2 % level, we have identified several factors which likely contributed to measurement bias in these prior studies. First, the previous measurements were acquired using different samples over a wide range of pressure, and spectra were fit using various line profiles both with [18,19,23] and without [21,22,24,25,29,30,32] line mixing. It is well documented that the choice of fitting line profile [40] and line mixing model [18] can affect the reported line intensity. Second, the recently documented effect of collision-induced intensity depletion in line cores and redistribution to a broad continuum [41–43] was not considered in any of the analyses. Third, at the time the FS-CRDS measurements [22,29,30] were made, NIST was unaware of any significant biases caused by non-ideality in commercial digitizers used to record the ring-down decay signals [44]. Fourth, relative uncertainty in the pathlength of the FTS and TDL measurements, 0.1 % to 0.2 % (where reported [18,19,23,32]), and the pressure uncertainty in all measurements, 0.1 % to 0.5 %, puts a lower bound on the uncertainty in previously reported measured intensities.

To mitigate these confounding effects, we restricted the present results to new FS-CRDS measurements. These data were acquired at relatively low pressures (< 1.35 kPa) for which the spectra were dominated by Doppler broadening, and for which effective pathlength uncertainties were miniscule. Operation at low pressure also minimized complications from line blending, and higher order collisional effects (*e.g.*, line mixing, CIA, and intensity depletion). We also used pure O_2 samples to reduce uncertainty in sample chemical composition, and we used a secondary pressure transfer standard to minimize and accurately quantify impacts of the pressure uncertainty on the molecular density. Finally, we incorporated two redundant metrology-grade digitizers in the FS-CRDS setup to reduce bias in measured ring-down decay rates [44]. As discussed below, these improvements to the experiment result in relative combined standard uncertainties in measured intensities at the 0.15 % level out to $J = 40$.

In the remainder of this article, we compare traditional analytical models [31,45,46] and a recent set of *ab initio* calculations of the line intensities [47]. Next, we describe the experimental method and results, providing line intensities and combined uncertainties for rotational quantum numbers up to $J = 40$. Using the predicted rotational dependence combined with the band intensity scaled in terms of the measured values, we present a line list for the O_2 A-band to $J = 60$. Finally, we compare our intensities with literature values, identifying statistically significant bias in certain cases and resulting in more realistic combined uncertainties incorporating both statistical and systematic contributions.

2. Theoretical models of O_2 A-band intensities

2.1. Herman-Wallis Watson (HWW) intensity model

We begin with a general expression for intensities of O_2 rovibronic bands based on Eq. 11 of Gamache et al. [45]. After accounting for the appropriate degeneracy factors for the $^{16}O_2$ A-band, the observed intensity of transition, $J'' \rightarrow J'$ with lower-state energy $E_{J''}$ at wavenumber $\nu_{J'' \rightarrow J'}$ is,

$$S_{J''\rightarrow J'}(T) = \frac{I_a}{8\pi c}\frac{\nu_{J''\rightarrow J'}}{\nu_{X\rightarrow b}^3}\,A_{X\rightarrow b}L_{J''\rightarrow J'}e^{-c_2E_{J'}/T}\left(1-e^{-c_2\nu_{J''\rightarrow J'}/T}\right)Q^{-1}(T), \tag{1}$$

in which I_a is the relative abundance of the $^{16}O_2$ isotopologue, J'' and $J'$are the lower and upper state total angular momentum quantum numbers, respectively, $\nu_{J'' \rightarrow J'}$ is the wavenumber of the transition, $A_{X \rightarrow b}$ is the integrated spontaneous emission (*i.e.*, Einstein A) coefficient for the $X \rightarrow b$ electronic transition with a wavenumber at band center of $\nu_{X \rightarrow b}$ and $L_{J'' \rightarrow J'}$ is the dimensionless Hönl-London factor accounting for the $J'' \rightarrow J'$ dependence of the transition moment squared [45]. The dependence of the intensity on temperature, T, is completely described by the product of the last three terms in Eq. (1). The first two quantities involve the Boltzmann term and the stimulated emission term, containing the conversion from wavenumber to temperature, $c_2 = hc/k$, in terms of the Planck constant, the speed of light and the Boltzmann constant. The third term depending on temperature is the total internal partition function equaling the product of the respective electronic, vibrational, and rotational terms, $Q(T) = Q_{elec}(T)Q_{vib}(T)Q_{rot}(T)$. Here, the Watson intensity model corresponds to the case where the HL factors, $L^{(W)}_{J''\rightarrow J'}$ derived by Watson [31] are used. Note that the transition-specific spontaneous emission coefficient, $A_{J' \rightarrow J''}$is given by $A_{X \rightarrow b}L_{J'' \rightarrow J'}$.

The O_2 A-band is a doubly forbidden, magnetic dipole-allowed transition [48]. Because the ground state is a triplet state, the total angular momentum quantum numbers of the rotational states with fine structure are $J = (N + S)$, whereas with the upper level being a singlet state, the rotational states with fine structure satisfy $J = N$. Here, N is the rotational angular momentum and S (not to be confused with the intensity above) represents the spin angular momentum. Each transition is specified by $\Delta NN''\Delta JJ''$, corresponding to four allowed branches denoted by PP, PQ, RR, and RQ, where P, Q, and R indicate ΔN and ΔJ for values of (-1, 0, 1), respectively. To simplify, we also specify a total angular momentum index, $m = -J''$ for the PP and PQ branch transitions ($\Delta N = -1$) and $m = J'' + 1$for those in the RR and RQ branches ($\Delta N = 1$).

A Herman-Wallis formula of the form [46],

$$F_{HW}(m) = \left(1 + a_1m + a_2m^2\right)^2, \tag{2}$$

historically has been used to treat vibration-rotation interactions occurring within the ground state of diatomic molecules. Although not strictly applicable in the present case, this modification to the Watson intensity model has also been applied in the analysis of O_2 A-band intensities [18,19,30]. Combining Eqs. (1) and (2), we define the Herman-Wallis-modified Watson (HWW) intensity model as

$$S^{(HWW)}_m(T) = F_{HW}(m)\frac{I_a}{8\pi c}\frac{\nu_m}{\nu_{X\rightarrow b}^3}\,A_{X\rightarrow b}L^{(W)}_m e^{-c_2E_m/T}\left(1-e^{-c_2\nu_m/T}\right)Q^{-1}(T), \tag{3}$$

where the total angular momentum quantum number indices, J'' and $J'$are replaced with m.

2.2. Ab initio methods

Somogyi et al. recently reported theoretical line intensities for the $^{16}O_2$ A-band [47] computed using the variational diatomic code Duo [49] with the newly developed modules for the magnetic [47] and quadrupole [50] intensities. They used a spectroscopic model consisting of potential energy (PE), spin-orbit (SO), electronic angular momentum (EAM) and quadrupole moment (QM) curves covering seven electronic states of O_2, $X^3\Sigma_g^-$, $a^1\Delta_g$, $b^1\Sigma_g^+$, $I^1\Pi_g$, $II^1\Pi_g$, $I^3\Pi_g$ calculated using the ic-MRCI/ aug-cc-pV5Z level of theory [47,50]. Some PE, SO and EAM curves (states $X^3\Sigma_g^-$, $a^1\Delta_g$ and $b^1\Sigma_g^+$) were optimized by fitting to the experimentally derived (MARVEL) energies of O_2 [51], while some other SO, EAM and QM curves (connecting with states $I^1\Pi_g$, $II^1\Pi_g$, $I^3\Pi_g$) were optimized [52] to the HITRAN 2020 band intensities of O_2. These are the first intensity calculations of O_2 from first principles and are therefore believed to describe the relative intensities (*i.e.*, the rotational dependence of the line intensities) more correctly than the effective or empirical expressions, see, *e.g.* [31]. Indeed, the A-band intensities of O_2 are formed from a complex interplay between the rovibronic matrix elements of SO, EAM and QM contributions associated with (at least) seven electronic states $X^3\Sigma_g^-$, $a^1\Delta_g$, $b^1\Sigma_g^+$, $I^1\Pi_g$, $II^1\Pi_g$, $I^3\Pi_g$ and the corresponding PE curves [47]. The complexity of the model and the lack of the experimental data required for the description of all these contributions make the problem of the intensities of O_2 from first principles challenging.

2.3. Comparison between Watson and ab initio models for m dependence of intensity

To quantify differences between the two theoretical approaches described above, we evaluate the relative m dependence of the intensities provided by the Watson model and *ab initio* calculations. Because the *ab initio* calculations provide $A^{(ai)}_m = A_{X\rightarrow b}L^{(ai)}_m$, the m dependence of the HL factor can be evaluated from the Einstein A coefficient given by the *ab initio* calculations, $A^{(ai)}_m$, according to

$$L^{(ai)}_m = Cd_\epsilon(2J'+1)\frac{A^{(ai)}_m}{A_{X\rightarrow b}}\frac{\nu_m^3}{\nu_{X\rightarrow b}^3}, \tag{4}$$

where $d_\epsilon = 3$ is the degeneracy of the ground state, and C is a constant normalization factor embedded in the HL factors (nominally equal toπ^2) so that $L^{(ai)}_{m=2}$ equals the minimum value $L^{(W)}_{m=2} = ½$ which occurs for the R1R1 transition. With this definition, the m dependence of the intensity ratio for the two cases is

$$r^{(ai-W)}_m = \frac{S^{(ai)}_m}{S^{(W)}_m} = \frac{L^{(ai)}_m}{L^{(W)}_m} = Cd_\epsilon(2J'+1)\frac{A^{(ai)}_m}{A_{X\rightarrow b}}\frac{\nu_m^3}{\nu_{X\rightarrow b}^3}\frac{1}{L^{(W)}_m}, \tag{5}$$

which is independent of temperature and is a function of intrinsic molecular properties. We also note that nearly identical values for $r^{(ai-W)}_m$ (relative differences of $< 2\times10^{-9}$) are be obtained by evaluating the ratio from $S_{J'' \rightarrow J'}\left[\nu_{X \rightarrow b}/\nu_{J'' \rightarrow J'}\right]Q(T)/\left[e^{-c_2E_m/T}\left(1-e^{-c_2\nu_m/T}\right)\right]$ using the *ab initio* intensities and normalizing as above. From Eq. (8) of Gamache et al. [45] and assuming $Q(T) \cong Q_{rot}(T)$, this expression is proportional to the product $A_{X \rightarrow b}L_{J'' \rightarrow J'}$ which is independent of temperature.

Using the *ab initio* values, $A^{(ai)}_m$ and the Watson values, $L^{(W)}_m$, gives the results for the calculated intensity ratio, $r^{(ai-W)}_m$, shown in Fig. 1. This

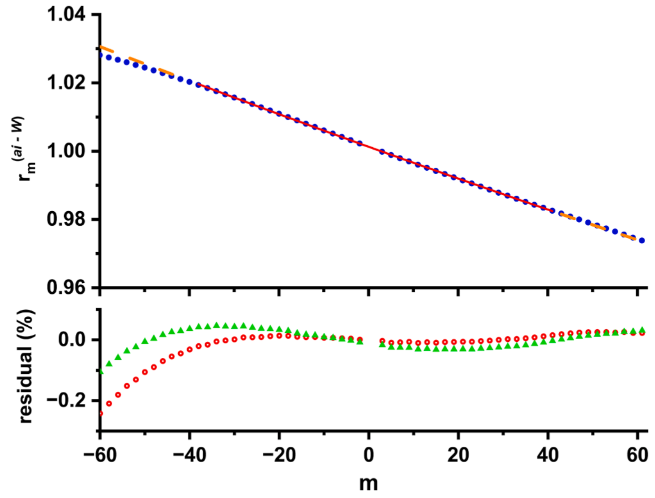

Fig. 1. Upper panel: ratio of intensities in the PQ and RQ branches predicted by *ab initio* model [47] and Watson model [31,45] (blue dots). The solid red line is a three-parameter fit of $a_0F_{HW}(m)$ to this result over the range $a_0F_{HW}(m)$ and the dashed orange lines are extrapolations of the fit, where $a_0 = 1.00129$, $a_1 = -2.35283\times10^{-4}$, and $a_2 = 1.15735\times10^{-7}$. The bottom panel shows the relative deviation between the extrapolated fit and the *ab initio* values (red circles), and the analogous fit residuals (green triangles) with a two-parameter fit with a_2 set to 0, and $a_0 = 1.00140$ and $a_1 = -2.29755\times10^{-4}$.

ratio was calculated only for the PQ and RQ branches, which, as will be shown below, provides the best agreement between experiment and *ab initio* theory. Over the range m = -60 to 60, $r_m^{(ai-W)}$ varies nearly linearly about unity by about ± 2.7 % from 1.028 to 0.974. This amount corresponds to the amount of "correction" (*i.e., $F_{HW}(m)$*) needed to ensure agreement between the HWW and *ab initio* models. The red line in the upper panel corresponds to a fit of $a_0F_{HW}(m)$ to the calculated $r_m^{(ai-W)}$, where a_0 is a fitted scaling factor close to unity. To simulate experimental conditions and assess uncertainty introduced by extrapolation with$F_{HW}(m)$, the fit was done over the range m = -38 to 41. The residuals, shown in the bottom panel, reveal a more than 0.2 % bias out to m = -60 in the extrapolated fit. As shown in the bottom panel of Fig. 1, setting the a_2 term to 0 only slightly changes the result. Treating the *ab initio* calculations as a proxy for true line intensities, in the absence of prior knowledge of the intensities beyond the measurement region, it is apparent that using Eq. (2) to extrapolate the results can lead to bias and uncertainty in the intensities.

3. Description of experiment and measurement results

3.1. Cavity ring-down spectrometer and gas sampling

All spectra were acquired at NIST in Gaithersburg, Maryland, USA with a custom-built spectrometer based on the FS-CRDS technique [53]. A total of 72 $^{16}O_2$ A-band transitions up to J = 40 were collected on room-temperature samples. The system uses the frequency-agile rapid scanning (FARS) [54,55] method for rapidly scanning the probe laser from mode-to-mode of the ring-down cavity and across a 20 GHz region centered about each target spectral transition. Fig. 2 presents a schematic of the experimental setup.

The optical cavity comprises two dual-coated, 760 nm (R = 99.98 %) and 633 nm (R = 95 %) high-reflectivity mirrors separated by nominally 75 cm, giving an effective path length of 3.5 km and finesse of 1.5×10^4. The observed ring-down time constants ranged from 4 μs to 12 μs. The free spectral range of the empty cavity was measured to be 198.8938 (15) MHz. The ring-down mirrors and piezoelectric assembly reside within an evacuable dumbbell-shaped enclosure forming the gas sample cell, with the long central portion being a 1.25 cm outer diameter electropolished stainless steel tube.

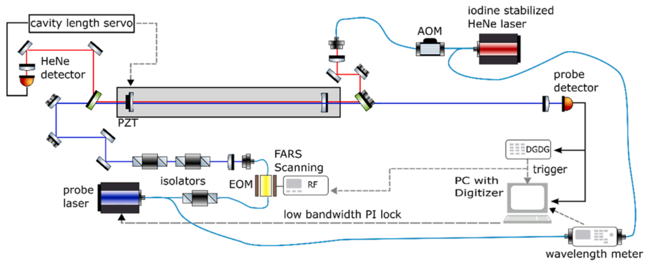

Fig 2. Schematic of spectrometer system used for frequency-stabilized cavity ring-down spectroscopy (FS-CRDS) measurements of the O_2 A-band. Abbreviations: electro-optic modulator (EOM), frequency-agile rapid scanning (FARS scanning), radiofrequency source (RF), digital gate and delay generator (DGDG), personal computer (PC), acousto-optic modulator (AOM).

One ring-down cavity mirror was mounted to a piezoelectric transducer that provides active stabilization of the ring-down cavity length through a proportional-integral-derivative (PID) servo that maintains resonance of an iodine-stabilized HeNe laser with a frequency stability of 12 kHz [39,40]. This reference laser is also used to calibrate the high-precision wavelength meter (~ 1 MHz) at the end of every FARS scan, providing an uncertainty in the absolute probe laser frequency of 30 MHz.

The probe laser is an external cavity diode laser (ECDL) with a wavelength tuning range from 755 nm to 772 nm and an output power of approximately 20 mW coupled into an optical fiber. A portion of the laser light is sent to the wavelength meter, while the other portion is directed through an optical isolator and then coupled into an electro-optic modulator (EOM). The output of the EOM is then launched into free space and passed through optical isolators. The beam is steered through mode-matching optics and coupled into the optical cavity, and the cavity transmission is collected on a silicon-based photoreceiver.

For a given FARS scan, the carrier frequency is stabilized with respect to the wavelength meter through another PID servo using current and piezo modulation of the ECDL [56]. The EOM is used to generate first-order sidebands, one of which is resonant with the cavity. When the cavity transmission reaches a defined threshold, a digital gate and delay generator (DGDG) sends a TTL pulse to a fast microwave switch to turn off the sideband generation. The pulse is also sent to the digitizer to trigger the cavity ring-down decay signal collection. Importantly, this experiment used a metrology-grade digitizer with a 20-bit resolution at 5 MS/s bandwidth. Using this type of digitizer ensures that nonlinear distortion effects that bias the measured decay rates are less than 0.02 % [44]. A subset of the measurements was made with a second metrology grade digitizer to verify consistent results.

This experiment used two pressure gauges with full scale ranges of 1.3 kPa and 133 kPa, respectively. The gauges were calibrated against a secondary pressure transfer standard (SPTS), which provides a link to the NIST primary pressure standard [57]. Because each step in the calibration chain increases the uncertainty in the pressure calibration, for one set of measurements, it was necessary to use the SPTS directly to measure the sample pressure.

The temperature was measured by a calibrated platinum resistance thermometer (PRT) in thermal contact with the outer surface of the sample tube and located midway between the two ring-down cavity mirrors. Temperature stability was improved by housing the sample cell/ring-down cavity assembly within an insulated enclosure. Additionally, ten thermocouples were fabricated and installed along the cell length. The reference probe of each thermocouple was co-located with the PRT, providing a real-time measurement of the temperature gradients across the cavity. These data provided the capability to correct the PRT temperature to the mean sample temperature.

Most data were collected in the pressure range 0.04 kPa to 1 kPa with an ultrahigh purity sample of O_2 (99.997 %). The relative abundance of the $^{16}O^{16}O$ molecular oxygen isotopologue was estimated to deviate by less than 0.2 ‰ from the HITRAN reference value (I_a= 0.995262) for this species [58]. Measurements were made at low pressures to enable using pure O_2 samples and to work in a domain where the lines are essentially Doppler broadened and impacts from higher-order collisional effects are minimal. Higher pressure data, up to 13.3 kPa, were also included for relatively weak high J transitions to compensate for the diminishing signal-to-noise ratio in the measured spectra.

Sample stability studies were conducted at the lowest operational pressure to determine when leaks in the system were large enough to be detectable. This threshold was given in terms of changes in the measured absorption above the noise floor and was found to be greater than 1 h. We found that the fill-to-fill variability was much larger than the statistical variation in replicate measurements on the same sample. A measurement cycle consisted of cavity evacuation with a turbo pump (for at least 8 min), then filling the cell with the O_2 sample, and measurement of two to three lines on a given sample where the time interval between the cavity filling and last spectrum measurement was less than 1 h. We also conducted measurements in three discrete data sets: (1) 1.3 kPa and 133.3 kPa pressure gauges with the primary metrology grade digitizer, (2) 1.3 kPa pressure gauge with the second metrology-grade digitizer, and (3) SPTS pressure gauge with the primary metrology-grade digitizer. Each dataset had 3 to 5 replicates per line, resulting in 900 unique line intensity measurements.

3.2. Measurement analysis, representative spectra, and quantification of uncertainty

Spectra collected at pressures below 1 kPa were fit individually using the Nelkin-Ghatak (NG) profile to capture Dicke narrowing effects, while spectra collected above this pressure were fit with the speed-dependent Nelkin-Ghatak (SDNG) profile. Both profiles are limiting cases of the Hartmann-Tran (HT) profile, which was recommended as the reference line profile for high-resolution molecular transitions [59]. All fits were made individually on each spectrum using the Multi-spectrum Analysis Tool for Spectroscopy (MATS) Python software package [60]. The spectra are modeled assuming absorption by $^{16}O_2$, where $\tau(\nu)$ is the ring-down time constant at cavity resonance frequency, ν, c is the speed of light, $\alpha(\nu)$is the absorption coefficient, ρ is the total number density (based on the ideal gas law at the measured pressure, p_{obs}, and temperature T_{obs}) of the gas (here assumed to be pure O_2), $S_m(T_{obs})$ is the observed intensity of transition having total angular momentum index, m, Φ_m is the normalized line profile (NG or SDNG) centered at line position ν_m, L_b is a linear baseline, and L_{et} are sinusoidal features in the baseline caused by etalons. The etalons are treated using an FFT filter of initial fit residuals in the frequency domain followed by inverse Fourier transformation. Specifying $\alpha_{b+et} = L_b + L_{et}$, then the measured spectrum of a single transition is modeled by,

$$[c\tau(\nu)]^{-1} = \alpha(\nu) + \alpha_{b+et} = \rho S_m(T_{obs})\Phi_m(\nu_m; T_{obs},\ p_{obs}) + L_b + L_{et}, \qquad (6)$$

where it is understood that any blending by nearby O_2 lines was described by additional terms $\rho S_{m'}(T_{obs})\Phi_{m'}(\nu_{m'}; T_{obs}, p_{obs})$ specified by m'.

Each measured intensity was obtained by fitting Eq. (6) to the measured spectrum $[c\tau(\nu)]^{-1}$, and floating the peak area equal to $p_{obs}(kT_{obs})^{-1}S_m(T_{obs})$. A typical absorption spectrum and its associated fit are shown in Fig. 3, in which the root-mean-square of the fit residuals is nearly four orders of magnitude smaller than the peak absorption. Using Eq. (1), each measured intensity at the T_{obs} was converted to intensity $S_m(T_r)$ at the reference temperature, $T_r = 296$ K, according to

$$S_m(T_r) = S_m(T_{obs})\frac{Q(T)}{Q(T_r)}\ \frac{e^{-c_2E''_m/T_r}\left(1 - e^{-c_2\nu_m/T_r}\right)}{e^{-c_2E''_m/T_{obs}}\left(1 - e^{-c_2\nu_m/\ T_{obs}}\right)}. \qquad (7)$$

The reported line intensities are based on the weighted average of the measured values determined from replicate spectra collected across several months and using unique sample fills. The replicates were averaged with weighting factors, $w_i = 1/\sigma_i^2$, where σ_i is the combined uncertainty based on the quadrature sum of the Type A (statistical) and Type B (systematic) evaluations of uncertainty. Because the pressure and temperature uncertainty varied across datasets, the quadrature sum of the statistical and systematic uncertainties were used to weight these data. The standard uncertainty components are summarized in Table 1. The measured line intensities (Table 3) include line-by-line statistical and combined uncertainties. In this instance, the line-by-line Type A uncertainty evaluation is a quadrature sum of the average fit uncertainty for the transition and the weighted standard deviation across the replicates for the transition. The combined uncertainty for each line is the weighted average of the statistical and systematic uncertainties for the replicate measurements of a transition.

The known systematic uncertainties arise from the sample impurity, isotopologue composition of the O_2, digitizer, choice of the line profile,

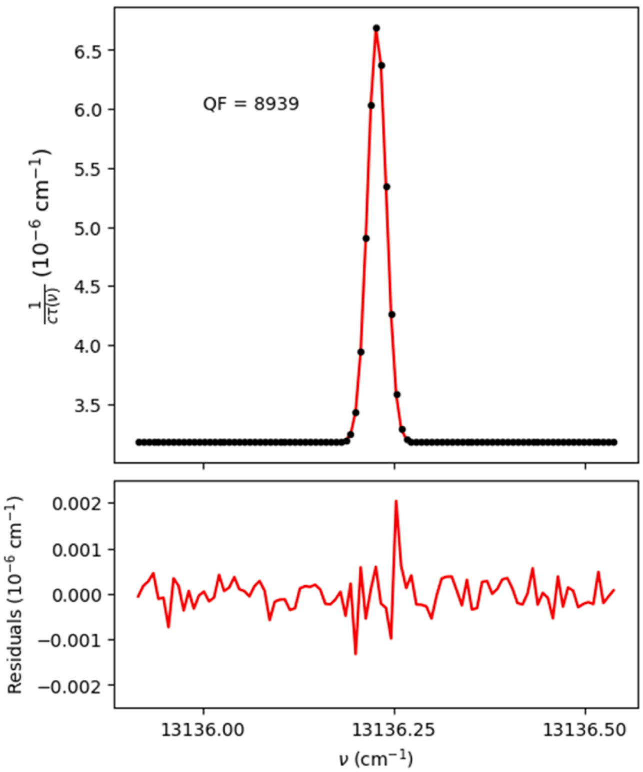

Fig. 3. Upper panel: FS-CRDS absorption spectrum (solid circles) and NGP fit (line) of the R5R5 $^{16}O_2$ A-band transition acquired on a sample of pure O_2 at room temperature and at a pressure $p_{obs} = 66.7$ Pa, using the spectrometer system described in Fig. 2. Here QF is the quality factor defined as the peak absorption divided by the root-mean-square of the fit residuals. Bottom panel: Fit residuals (measurement – fit).

Table 1
Standard relative uncertainty components for FS-CRDS line intensity measurements. Statistical and combined uncertainties for each transition are provided in Table 3.

Evaluation Type	component	u_r (%)
A	spectrum fit uncertainty	0.02 (median)
A	sampling repeatability	0.03 (median)
B	sample composition	0.003
B	$^{16}O_2$ relative isotopic abundance	0.02
B	lineshape	0.002
B	digitizer uncertainty	< 0.03
B	internal partition function	< 0.02
B	temperature	0.03 (average)
B	pressure	0.11 (average)
B	intensity depletion	0.005 (average)

intensity depletion associated with breakdown of the impact approximation [41–43], partition function, cavity mode spacing, temperature, and pressure. The sample composition uncertainty is less than 0.003 %, as reported from the certificate of batch analysis from the manufacturer [61]. The difference in back-to-back measurements with the primary and secondary metrology-grade digitizers was used to estimate digitizer-driven uncertainty in measurement of the decay rate. The difference was less than sampling repeatability ($<$ 0.03 %). We estimated uncertainty associated with the choice of line profile by comparing NG and SDNG profile fits to the data of the P7P7 line. This estimate does not include any inherent bias between these HT-derived line profiles and the spectrum line shape, although given the proximity of the measurements to the Doppler limit, these deviations are expected to be well below 0.1 % [62]. These measurements were collected at low pressures to allow the use of pure O_2 samples and to operate in a regime where impacts of higher-pressure effects are small. The intensity depletion effect was also considered as a source of error. For each line, we estimate the bias introduced by neglecting this effect in terms of the measured pressure and the calculated (based on classical molecular dynamics simulations) intensity depletion coefficient at room temperature for air-broadened O_2 [63]. The uncertainty in the partition function is based on the changes between the Total internal partition sums (TIPS) 2011 and 2017 versions at 296 K for O_2 [64]. The uncertainty in the pressure measurement is evaluated from the root-mean-square sum of the variation during the measurement, the calibration uncertainty, the pressure calibration drift, and the uncertainty in the zero-pressure measurement. Similarly, the temperature uncertainty is calculated from the calibration uncertainty, uncertainty in the gradient correction, and the deviation during the measurement. These uncertainties are obtained by quadrature addition of the partial derivatives with respect to pressure and temperature (obtained from Eqs. (6) and (7)) multiplied by the uncertainty in the respective parameters [65].

4. Comparison of experiment and theory

4.1. Scaling of the ab initio intensity model

In recent measurements of CO_2 line intensities, Long et al. [66] and Fleurbaey et al. [67] modeled the J dependence of the measured intensities using a band-intensity-scaled *ab initio* line-by-line spectroscopic model. In the case of several near-IR rovibrational CO_2 bands, they found that these theoretical line intensities adequately captured the J dependence of the measured intensities to within the measurement precision. Consequently, a single scaling factor specified as β, was sufficient to scale the calculated integrated band intensity to match the observations [66,67]. Notably, in the present study we take this same approach despite finding that the present β factor differs from unity by a much greater amount compared to the β factors recovered from measurements of these CO_2 bands [66,67]. We attribute this discrepancy to shortcomings of the *ab initio* model in terms of accurate prediction of the O_2 A-band integrated intensity. Nevertheless, as shown below, the relative J dependence of the *ab initio* calculation is in excellent agreement with the present measured spectra.

Intensity scaling of the *ab initio* results for the O_2 A-band (Section 2.2) provides several advantages over the HWW band intensity model given by Eq. (3). First, these *ab initio* calculations account for physical effects that are not described by the HL factors used in the Watson model and for which the HW modification is not strictly justified. Second, provided that the relative values of the *ab initio* intensities have been validated over a sufficiently wide range of J, then these calculations can be extrapolated to higher J values, thus extending the results to difficult-to-measure weak transitions. Finally, because the fitted scaling factor, β, is J independent, then relative uncertainty in the extrapolated intensities as well as that of the band intensity equals the relative uncertainty in β – with the caveat that extrapolation of this *ab initio* model is physically justified and does not introduce significant additional uncertainty.

Fig. 4 summarizes the results obtained in this scaling of the *ab initio* line intensities. Most notably, the relative line intensities agree well in the PQ- and RQ-branches, whereas there are significant systematic deviations outside the statistical experimental uncertainties for the PP- and RR-branches. Note that at low J the systematic uncertainty is the dominant component of the combined uncertainty, but at high J the statistical uncertainties dominate based on the diminishing signal-to-noise ratio of the measured transitions.

Differences between the experimental and *ab initio* J dependences in the PP and RR branches can be ascribed to branch-dependent differences in different intensity components such as quadrupole, spin-orbit and electronic angular momentum (L-uncoupling) which will be addressed by future refinements to the theoretical calculations.

However, in the interim, we have made an empirical correction to the theoretical intensities in these two branches based on the β scaling factor obtained by a constrained fitting procedure. The scaling parameter, β, is obtained by fitting Eq. (8) to measured intensities only in the PQ- and RQ-branches. We introduce a single-parameter linear correction term, b, to account for the slight discrepancy between experiment and theory in in the PP- and RR-branches (see Eq. (9)), where the deviations have odd symmetry about the band center. Thus, the relation between the measured, S_m, and theoretical *ab initio*, $S_{m,ai}$, intensities for the PQ- and RQ-branches is given by,

$$S_m = \beta S_{m,ai}, \tag{8}$$

whereas for the PP- and RR-branches we assume

$$S_m = \beta S_{m,ai}(1 + bm). \tag{9}$$

Fig. 5 shows the results (see Table 2 for resulting fit parameters and uncertainties) obtained by scaling the *ab initio* intensities to the measured values. The results are extrapolated to $J = 60$ and reveal that the PP-branch and RR-branch correction term, b, introduces an uncertainty that grows linearly with $|m|$, but only for the intensities within these two branches. However, it greatly improves the agreement between theory and measurement to within the statistical uncertainty of the measurements. Summation of the scaled *ab initio* intensities over the

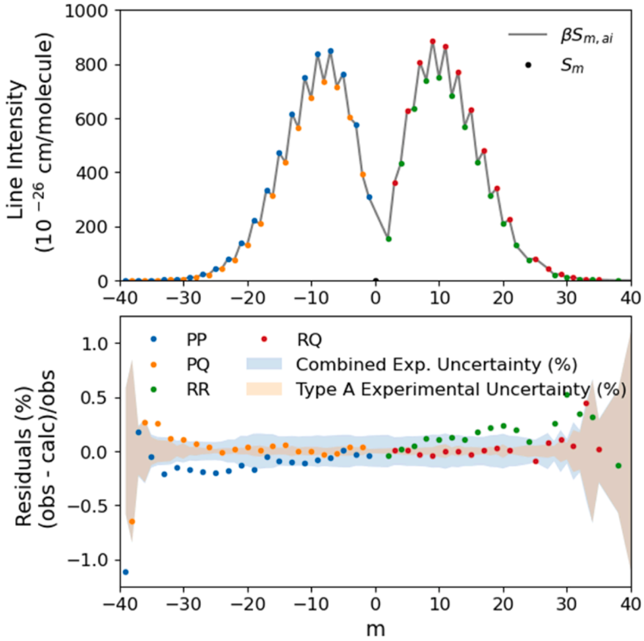

Fig. 4. Intensity scaling of *ab initio* intensities [47] in terms of measured values. Top: Line intensities from the experiment (circles) and scaled *ab initio* spectroscopic model (line). Bottom: Residuals from *ab initio* spectroscopic model fit to experimental data separated by sub-branches, where the shaded regions correspond to the experimental uncertainties.

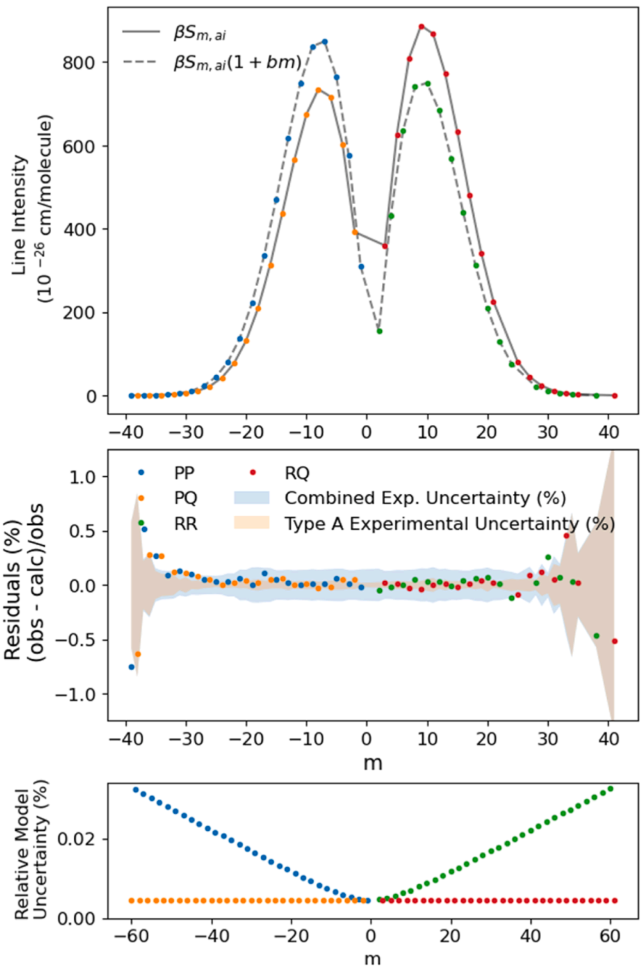

Fig. 5. Model and residuals for *ab initio* intensities scaled by β (PQ- and RQ-branches) and those scaled by β with linear correction b (PP- and RR-branches) after fits to measured intensities. Top panel: Line intensities from the experiment (circles) and scaled *ab initio* spectroscopic model (PQ/RQ solid line and PP/RR dashed line) with residuals in the middle panel. Bottom panel: Relative model uncertainty from *ab initio* spectroscopic model fit to experimental data separated by sub-branch.

Table 2
Band intensity parameters for the scaled *ab initio* intensity model with linear correction. In the *ab initio* scaled intensity model the band intensity, S_b, is not a floated parameter but is instead determined from the sum of intensities up to $J = 60$ with the reported relative uncertainty, u_r, in parentheses resulting from the sum of the combined standard uncertainties. The reported uncertainties in the β and b parameters are as reported from the fit.

parameter	units	scaled *ab initio* intensity model
S_b	(cm molecule^{-1})	2.2496×10^{-22} ($u_R = 0.14$ %)
β		0.87981(4)
b		$8.90(54) \times 10^{-5}$

range of tabulated J values gives a band intensity, S_b, of 2.2496×10^{-22} cm molecule^{-1}, with a relative combined standard uncertainty of 0.14 %. This value represents a lower bound on our reported band intensity uncertainty.

In our scaling of the *ab initio* intensity model to the experimental results, the line intensity measurements were weighted using the following normalized factors given by

$$w_m = \frac{1}{\sigma_m^2}\frac{1}{\sum_m \frac{1}{\sigma_m^2}}, \tag{10}$$

where σ_m is the relative combined uncertainty in the average measured line intensity for a transition. The uncertainty in the *ab initio* band intensity model was evaluated by incorporating the statistical uncertainties in the fitted parameters, β and *b*. We note that the resulting statistical uncertainty in the scaled *ab initio* model does not include uncertainty in the underlying *m* dependence of the intensities caused by deficiencies in implementation of the *ab initio* theory. Our model uncertainties also include the systematic measurement uncertainties. For the transitions that were not measured, the systematic uncertainties are reported as the average of all those that were measured.

The isotopically weighted measured and scaled *ab initio* intensities, uncertainties, and non-isotopically weighted Einstein A coefficients are summarized in Table 3 where we give the theoretical results for lines with assignments from P61Q60 to R59Q60. These results extend the tabulated intensities more than six orders of magnitude from $S_m = 1.23\times10^{-27}$ cm molecule^{-1} for the weakest measured transition (P39P39) to $S_m = 4.46\times10^{-34}$ cm molecule^{-1} (P61Q60). To quantify the agreement between the experimental and theoretical J dependence of the intensities, we calculated the distribution of relative differences between these values for the PQ- and RQ-branch data comprising 36 measured lines. This analysis gives a one standard deviation value equal to 0.18 % (all lines), 0.03 % (22 relatively strong lines from P25Q24 to R19Q20), and an average relative difference of 0.12 % for all lines with each datum weighted by the corresponding reciprocal combined variance.

4.3. *Comparison between the HWW and scaled ab initio models*

For completeness, we also compared the HWW model fit to the measured intensity and the scaled *ab initio* model discussed above. These results are discussed in the Supplementary Materials and reveal branch-dependent differences between the resulting extrapolated intensities using the HWW and scaled *ab initio* models.

4.4. *Comparison to literature*

In Fig. 6 we present the relative differences between two sets of literature intensities (left and right panels) and the present scaled *ab initio* intensities which are essentially anchored to the present measurements, shown in the right panel. In the left panel (Set I) we include results from previous TDL [24] and FTS-based [21,23,25,32] measurements, and in the right panel (Set II) we summarize the results of higher-precision FS-CRDS experiments [22,29,30] as well as line intensities which were derived from FS-CRDS measurements and additional FTS measurements [18,19]. These three sets of O_2 A-band line intensities were archived in HITRAN 2012 [30,34], HITRAN 2016 [19, 37], and HITRAN 2020 [18,39], respectively.

It is apparent that the Set I results in Fig. 6, which includes intensities reported by Ritter and Wilkerson [24], Schermaul and Learner [25], Brown and Plymate [21], Predoi-Cross et al. [23], and Petrova et al. [32] on average are in good agreement with the present results, although these data have relatively large uncertainties by comparison to the higher-precision results, dominated by FS-CRDS measurements, in the Set II data. Nevertheless, given that experimental biases in all five sets of unrelated data (*e.g.*, pathlengths, temperature errors, line shape effects, *etc.*) are likely to be uncorrelated, averaging over these relatively low-precision measurements provides an interesting comparison. We find that for $|m| < 30$ the mean deviation with respect to the present results is 0.044 %, with a standard error in the mean of 0.43 %.

All Set II data in Fig. 6 have systematically different J dependences in the line intensities and smaller band intensities compared to this study. As discussed above, all FS-CRDS measurements [22,29,30] contributing to the results reported by Long et al. [30] and included in the combined FTS and FS-CRDS dataset used in Drouin et al. [19] and Payne et al. [18] would have been susceptible to unknown-at-the-time biases from the use

Table 3

Summary of line-by-line isotopically weighted ($I_a = 0.995262$) transition intensities, S_m, for the O_2 A-band in units of cm molecule^{-1}. The line-by-line statistical, u_r^A and combined, $u_r = \left[\left(u_r^A\right)^2 + \left(u_r^B\right)^2\right]^{1/2}$, relative standard uncertainties (in %) are provided for the measured values and for the scaled *ab initio* band intensities models. For the measured intensities, the u_r^A and $u_r$are based on those from Table 1. The uncertainties in the scaled *ab initio* intensities u_r^A are from the constrained parameter fit of β and b in Table 3, with u_r^B for each line given by the corresponding measurement uncertainty (with data present) and the average value (no data case). The Einstein A coefficients (in s^{-1}) are from the scaled *ab initio* intensities and were calculated as $A_m = 8\pi cQ(T_r)\nu_m^2 S_{m,\ ai}/\left[I_a(2J' + 1)e^{-E''_m c2/T_r}\left(1 - e^{-\nu_m c2/T_r}\right)\right]$.

		measured values			scaled *ab initio model*			
Line	m	S_m	u_r^A	u_r	$S_{m,ai}$	u_r^A	u_r	A_m
P61Q60	-60				4.46201E-34	0.005	0.12	0.021064
P59P59	-59				2.28244E-33	0.032	0.13	0.021621
P59Q58	-58				2.24743E-33	0.005	0.12	0.021139
P57P57	-57				1.09086E-32	0.031	0.13	0.021711
P57Q56	-56				1.07339E-32	0.005	0.12	0.021212
P55P55	-55				4.94222E-32	0.030	0.13	0.021800
P55Q54	-54				4.85977E-32	0.005	0.12	0.021283
P53P53	-53				2.12190E-31	0.029	0.13	0.021888
P53Q52	-52				2.08483E-31	0.005	0.12	0.021350
P51P51	-51				8.63064E-31	0.028	0.13	0.021976
P51Q50	-50				8.47272E-31	0.005	0.12	0.021415
P49P49	-49				3.32433E-30	0.027	0.13	0.022063
P49Q48	-48				3.26037E-30	0.005	0.12	0.021478
P47P47	-47				1.21214E-29	0.026	0.13	0.022149
P47Q46	-46				1.18768E-29	0.005	0.12	0.021539
P45P45	-45				4.18276E-29	0.025	0.13	0.022235
P45Q44	-44				4.09380E-29	0.005	0.12	0.021598
P43P43	-43				1.36542E-28	0.024	0.13	0.022323
P43Q42	-42				1.33469E-28	0.005	0.12	0.021653
P41P41	-41				4.21499E-28	0.023	0.13	0.022411
P41Q40	-40				4.11460E-28	0.005	0.12	0.021708
P39P39	-39	1.22075E-27	0.58	0.59	1.22999E-27	0.022	0.10	0.022502
P39Q38	-38	1.19125E-27	0.85	0.85	1.19885E-27	0.005	0.09	0.021761
P37P37	-37	3.40871E-27	0.22	0.24	3.39122E-27	0.021	0.09	0.022594
P37Q36	-36	3.30903E-27	0.29	0.3	3.29981E-27	0.005	0.09	0.021811
P35P35	-35	8.85481E-27	0.13	0.16	8.83117E-27	0.020	0.09	0.022690
P35Q34	-34	8.59996E-27	0.1	0.13	8.57707E-27	0.005	0.09	0.021861
P33P33	-33	2.17289E-26	0.1	0.13	2.17092E-26	0.018	0.09	0.022790
P33Q32	-32	2.10654E-26	0.09	0.13	2.10396E-26	0.005	0.09	0.021909
P31P31	-31	5.04207E-26	0.05	0.1	5.03533E-26	0.017	0.09	0.022896
P31Q30	-30	4.87382E-26	0.07	0.11	4.86817E-26	0.005	0.08	0.021956
P29P29	-29	1.10237E-25	0.04	0.09	1.10128E-25	0.016	0.08	0.023009
P29Q28	-28	1.06269E-25	0.04	0.09	1.06183E-25	0.005	0.08	0.022002
P27P27	-27	2.27099E-25	0.03	0.09	2.26971E-25	0.015	0.08	0.023131
P27Q26	-26	2.18252E-25	0.03	0.09	2.18140E-25	0.005	0.08	0.022047
P25P25	-25	4.40556E-25	0.02	0.09	4.40436E-25	0.014	0.08	0.023265
P25Q24	-24	4.21753E-25	0.03	0.09	4.21746E-25	0.005	0.09	0.022091
P23P23	-23	8.04281E-25	0.03	0.11	8.03996E-25	0.013	0.11	0.023416
P23Q22	-22	7.66762E-25	0.02	0.11	7.66556E-25	0.005	0.10	0.022137
P21P21	-21	1.37995E-24	0.03	0.14	1.37907E-24	0.012	0.14	0.023590
P21Q20	-20	1.30861E-24	0.03	0.14	1.30805E-24	0.005	0.14	0.022184
P19P19	-19	2.21951E-24	0.04	0.16	2.21938E-24	0.011	0.16	0.023791
P19Q18	-18	2.09238E-24	0.05	0.16	2.09199E-24	0.005	0.16	0.022232
P17P17	-17	3.34876E-24	0.04	0.16	3.34510E-24	0.010	0.15	0.024033
P17Q16	-16	3.13042E-24	0.03	0.16	3.12875E-24	0.005	0.15	0.022283
P15P15	-15	4.71279E-24	0.03	0.14	4.71035E-24	0.009	0.13	0.024334
P15Q14	-14	4.36562E-24	0.03	0.14	4.36285E-24	0.005	0.13	0.022340
P13P13	-13	6.17680E-24	0.05	0.14	6.17559E-24	0.008	0.13	0.024721
P13Q12	-12	5.64795E-24	0.03	0.14	5.64780E-24	0.005	0.13	0.022407
P11P11	-11	7.50179E-24	0.04	0.14	7.50177E-24	0.008	0.13	0.025247
P11Q10	-10	6.74357E-24	0.04	0.14	6.74296E-24	0.005	0.13	0.022489
P9P9	-9	8.37940E-24	0.04	0.15	8.37851E-24	0.007	0.14	0.026008
P9Q8	-8	7.34560E-24	0.03	0.14	7.34756E-24	0.005	0.14	0.022600
P7P7	-7	8.49651E-24	0.03	0.15	8.49580E-24	0.006	0.14	0.027226
P7Q6	-6	7.16945E-24	0.04	0.15	7.17056E-24	0.005	0.14	0.022767
P5P5	-5	7.64233E-24	0.04	0.15	7.63756E-24	0.005	0.14	0.029512
P5Q4	-4	6.02949E-24	0.04	0.15	6.02665E-24	0.005	0.14	0.023068
P3P3	-3	5.77178E-24	0.03	0.14	5.77130E-24	0.005	0.13	0.035432
P3Q2	-2	3.92430E-24	0.04	0.14	3.92238E-24	0.005	0.13	0.023846
P1P1	-1	3.09229E-24	0.02	0.14	3.09298E-24	0.005	0.14	0.088617
R1R1	2	1.54452E-24	0.03	0.15	1.54524E-24	0.005	0.15	0.008866
R1Q2	3	3.59972E-24	0.03	0.13	3.59905E-24	0.005	0.13	0.020468
R3R3	4	4.31989E-24	0.03	0.13	4.32045E-24	0.005	0.13	0.014780
R3Q4	5	6.26667E-24	0.04	0.14	6.26585E-24	0.005	0.13	0.021239
R5R5	6	6.34583E-24	0.03	0.14	6.34589E-24	0.006	0.13	0.017055
R5Q6	7	8.08413E-24	0.03	0.14	8.08633E-24	0.005	0.14	0.021531
R7R7	8	7.40796E-24	0.03	0.14	7.40390E-24	0.006	0.14	0.018260

(*continued on next page*)

Table 3 (*continued*)

		measured values			scaled *ab initio model*			
Line	m	S_m	u_r^A	u_r	$S_{m,ai}$	u_r^A	u_r	A_m
R7Q8	9	8.87333E-24	0.04	0.15	8.87639E-24	0.005	0.15	0.021685
R9R9	10	7.50449E-24	0.05	0.15	7.50232E-24	0.007	0.14	0.019005
R9Q10	11	8.68016E-24	0.06	0.16	8.67991E-24	0.005	0.15	0.021778
R11R11	12	6.83637E-24	0.03	0.15	6.83416E-24	0.008	0.14	0.019509
R11Q12	13	7.72583E-24	0.05	0.15	7.72517E-24	0.005	0.14	0.021840
R13R13	14	5.69277E-24	0.03	0.14	5.69317E-24	0.009	0.14	0.019872
R13Q14	15	6.32933E-24	0.04	0.14	6.33054E-24	0.005	0.13	0.021882
R15R15	16	4.38154E-24	0.03	0.13	4.37958E-24	0.010	0.13	0.020145
R15Q16	17	4.81154E-24	0.03	0.13	4.81082E-24	0.005	0.13	0.021911
R17R17	18	3.13193E-24	0.04	0.15	3.12991E-24	0.011	0.14	0.020356
R17Q18	19	3.40722E-24	0.03	0.15	3.40596E-24	0.005	0.15	0.021931
R19R19	20	2.08808E-24	0.06	0.16	2.08661E-24	0.012	0.15	0.020522
R19Q20	21	2.25422E-24	0.03	0.14	2.25378E-24	0.005	0.14	0.021944
R21R21	22	1.30151E-24	0.04	0.14	1.30141E-24	0.013	0.14	0.020655
R21Q22	23				1.39714E-24	0.005	0.12	0.021950
R23R23	24	7.60048E-25	0.06	0.12	7.60965E-25	0.014	0.11	0.020763
R23Q24	25	8.12160E-25	0.05	0.11	8.12848E-25	0.005	0.09	0.021952
R25R25	26				4.17824E-25	0.015	0.12	0.020850
R25Q26	27	4.44825E-25	0.06	0.17	4.44432E-25	0.005	0.16	0.021950
R27R27	28	2.15755E-25	0.05	0.1	2.15709E-25	0.016	0.08	0.020922
R27Q28	29	2.28891E-25	0.1	0.2	2.28622E-25	0.005	0.17	0.021944
R29R29	30	1.05092E-25	0.08	0.12	1.04815E-25	0.017	0.09	0.020979
R29Q30	31	1.10809E-25	0.19	0.27	1.10747E-25	0.005	0.19	0.021935
R31R31	32	4.80144E-26	0.17	0.2	4.79794E-26	0.018	0.10	0.021026
R31Q32	33	5.07897E-26	0.41	0.46	5.05571E-26	0.005	0.2	0.021922
R33R33	34	2.07106E-26	0.66	0.67	2.07048E-26	0.019	0.12	0.021063
R33Q34	35	2.17702E-26	0.29	0.3	2.17653E-26	0.005	0.09	0.021907
R35R35	36				8.42833E-27	0.020	0.13	0.021091
R35Q36	37				8.84160E-27	0.005	0.12	0.021888
R37R37	38	3.22333E-27	0.57	0.58	3.23822E-27	0.021	0.09	0.021111
R37Q38	39				3.39082E-27	0.005	0.12	0.021868
R39R39	40				1.17492E-27	0.022	0.13	0.021125
R39Q40	41	1.22189E-27	1.37	1.37	1.22826E-27	0.005	0.10	0.021844
R41R41	42				4.02750E-28	0.023	0.13	0.021132
R41Q42	43				4.20411E-28	0.005	0.12	0.021818
R43R43	44				1.30492E-28	0.024	0.13	0.021134
R43Q44	45				1.36030E-28	0.005	0.12	0.021789
R45R45	46				3.99764E-29	0.025	0.13	0.021130
R45Q46	47				4.16238E-29	0.005	0.12	0.021757
R47R47	48				1.15849E-29	0.026	0.13	0.021122
R47Q48	49				1.20491E-29	0.005	0.12	0.021722
R49R49	50				3.17691E-30	0.027	0.13	0.021109
R49Q50	51				3.30088E-30	0.005	0.12	0.021685
R51R51	52				8.24734E-31	0.028	0.13	0.021092
R51Q52	53				8.56093E-31	0.005	0.12	0.021645
R53R53	54				2.02737E-31	0.029	0.13	0.021069
R53Q54	55				2.10270E-31	0.005	0.12	0.021603
R55R55	56				4.72114E-32	0.030	0.13	0.021044
R55Q56	57				4.89287E-32	0.005	0.12	0.021558
R57R57	58				1.04180E-32	0.032	0.13	0.021013
R57Q58	59				1.07893E-32	0.005	0.12	0.021510
R59R59	60				2.17927E-33	0.033	0.13	0.020979
R59Q60	61				2.25555E-33	0.005	0.12	0.021460

of an uncalibrated or non-metrology-grade digitizer [44]. Other factors contributing to the discrepancy between these data and the present results include pressure-dependent intensity depletion as well as correlations between fitted parameters in the analysis of measurements spanning a wide pressure range. We expect that these effects could systematically alter the measurements of relative intensity (J dependence) as well as band intensity. A disadvantage of the HWW intensity model (used in Long et al. [30], Drouin et al. [19], and Payne et al. [18]) is that it allows for adjustment to fit high J behavior that may or may not have a spectroscopic origin. This flexibility can mask the effect of unidentified or poorly constrained mechanisms that contribute to structured residuals.

In Table 4 we present each literature (lit) band intensity, the relative difference with respect to this study (ts) defined as $\Delta s_b^{(lit)} = \left(S_b^{(lit)}/S_b^{(ts)}\right) - 1$, and a normalized difference parameter (NDP) defined as $\left|\Delta s_b^{(lit)}\right| / u_r^{(com)}$ where $u_r^{(com)} = \left[\left(u_r^{(lit)}\right)^2 + \left(u_r^{(ts)}\right)^2\right]^{1/2}$ is the relative combined standard uncertainty of the band intensity of the compared values. The more that NDP exceeds unity, the less probable that the difference in band intensities is consistent with both reported uncertainties. This NDP analysis shows that as the statistical uncertainty in the measurement improved from Set I to Set II the NDP rose above unity highlighting the importance of quantifying systematic uncertainty sources. Long et al. [30] reported a combined standard uncertainty in band intensity of 0.31 %, which may have been about a factor of two too small. The studies by Drouin et al. [19] and Payne et al. [18] report fit uncertainties, but do not report combined standard uncertainties. However, the studies note that the uncertainty in line intensity is limited by the pressure measurement; thus a $u_r(S_b) = 0.1$ % is used, consistent with the lower bound of the reported pressure uncertainties [19]. Payne et al. [18] reports the next iteration of the integrated self-consistent spectroscopic model reported in Drouin et al. [19], where a key

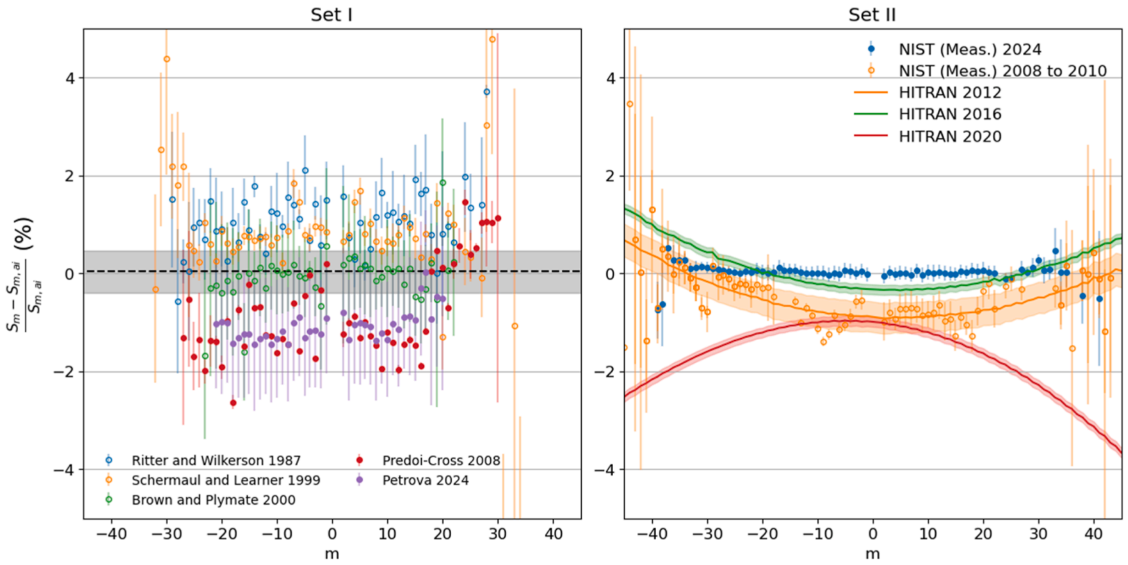

Fig. 6. Comparison of line intensities between literature data and the scaled *ab initio* calculations. Left (set I): Comparisons with literature tunable dye laser (TDL) [24] and Fourier transform spectroscopy (FTS) [21,23,25,32] data. The black dashed line represents the average difference from the *ab initio* scaled model, 0.04 %, with the shaded region representing the standard error of 0.4 %. Right (set II): Comparisons with NIST frequency-stabilized cavity ring-down spectroscopy (FS-CRDS) measurements 2008 to 2010 [22,29,30] and 2024 measurements and HITRAN 2012 to 2020 [18,19,30,34,37,39]. The shaded regions represent the uncertainties on the reported band intensity models.

Table 4
Band intensities and uncertainties in units of (10^{-22} cm molecule^{-1}) evaluated up to $|m| = 45$ for this work and the data shown in Fig. 6 for set I (second row) and set II (last three rows). The normalized difference parameter, NDP, defined as $|\Delta s_b| \ / u_r^{(com)}$, is determined by comparison to the present results. *The set I values are based on the average band intensities from the five data sets summed over $|m| \leq 30$, and corrected to $|m| = 45$ using the *ab initio* intensities by the ratio $\sum_{|m|\leq 45} S_{m.ai} / \sum_{|m|\leq 30} S_{m.ai} = 1.0018$. **The Drouin et al. [19] and Payne et al. [18] are set to 0.1 %, which is the lower bound of the reported pressure uncertainty [19].

	HITRAN version	S_b	$u(S_b)$	$u_r(S_b)$(%)	Δs_b (%)	$u_r^{(com)}$ (%)	$\lvert\Delta s_b\rvert/u_r^{(com)}$
this study		2.2496	0.0031	0.14			
Set I *		2.2506	0.0097	0.43	0.044	0.45	0.1
Long et al. [30]	2012	2.2314	0.0070	0.31	-0.81	0.34	2.4
Drouin et al. [19]	2016	2.2441	0.0022	0.10**	-0.24	0.17	1.5
Payne et al. [18]	2020	2.2234	0.0022	0.10**	-1.16	0.17	6.7

difference is the simultaneous adjustment of the HWW intensity and line mixing models. The large difference in NDP between the Payne et al. [18] and Drouin et al. [19], respectively 6.7 and 1.5, might be ascribed to biases due to correlations between line intensity and higher-pressure physics modeling.

By evaluating a weighted average of the literature band intensities from Sets I and II we determined a “best estimate” of $S_b^{(lit)}$ of data that were acquired prior to this study. In this analysis we use the standard error in the mean for the composite Set I data as discussed above, and for Set II we assign the uncertainties as the standard deviation of the three Δs_b values. Weighting all four literature band intensity values in Table 4 by the respective squares of the reciprocal uncertainties (0.43 % for Set I and 0.5 % for each case in Set II) gives an average value, $\Delta s_b^{(lit)} =$ -0.50 %. Given our comprehensive uncertainty analysis where statistical and systematic effects were considered, and because $|\Delta s_b^{(lit)}|$ exceeds our uncertainty by nearly a factor of four, this result is probably dominated by a negative bias in the prior best estimate of $S_b^{(lit)}$.

5. Conclusions

This work reports measured line intensities in the $^{16}O_2$ A-band for 72 transitions up to $J = 40$ with relative combined standard uncertainties at the 0.15 % level. These measurements were conducted at low pressures with pure O_2 samples to minimize complicating collisional effects and uncertainty in sample composition. The rotational quantum number dependence of the measured intensities and corresponding values obtained from *ab initio* calculations were in good agreement, especially in the PQ- and RQ-branches. Because the measured intensities were significantly more accurate than the *ab initio* band-integrated intensity, these theoretical calculations were scaled accordingly thus allowing accurate extrapolation of the intensities to $J = 60$.

Satellite measurements that use O_2 for retrieving atmospheric temperature profiles rely on accurate modeling of relative changes to the band shape [1–5]. The scaled *ab initio* line intensity model provides a physically based constraint to the relative band intensity compared to the previous empirical HWW model that should improve the ability to retrieve accurate temperature profiles. Low-uncertainty absolute line intensities are a key step in developing a self-consistent integrated O_2 A-band spectroscopic model necessary for airmass retrievals. Using the present experimental scaled *ab initio* line intensities can eliminate numerical correlations encountered in the retrieval of spectroscopic peak areas and line shape parameters for measurements made over a wide pressure range. Thus, the present results are expected to improve integrated models of the O_2 A-band where advanced line shapes, line-mixing, collision induced absorption and especially intensity depletion are important. Developing such a robust spectroscopic model is critical to minimizing uncertainties in satellite and remote sensing missions that use the O_2 A-band for measurements of airmass and mixing ratio of co-located greenhouse gases such as CO_2.

Supplementary material

Supplementary material associated with this article can be found, in the online version, at doi:XXXX

CRediT authorship contribution statement

Erin M. Adkins: Writing – review & editing, Writing – original draft, Visualization, Methodology, Investigation, Formal analysis, Data curation, Conceptualization. **Sergei N. Yurchenko:** Writing – original draft, Supervision, Data curation. **Wilfrid Somogyi:** Data curation. **Joseph T. Hodges:** Writing – review & editing, Writing – original draft, Supervision, Project administration, Funding acquisition, Formal analysis, Conceptualization.

Declaration of competing interest

The authors declare that they have no known competing financial interests or personal relationships that could have appeared to influence the work reported in this paper.

Acknowledgments

We acknowledge funding from the NIST Greenhouse Gas and Climate Science Program and the National Aeronautics and Space Administration (NASA) [contract NNH20ZDA0001N-OCOT]. The authors would like to thank David Long (NIST) and James Radney (NIST) for commenting on the manuscript.

Supplementary materials

Supplementary material associated with this article can be found, in the online version, at doi:10.1016/j.jqsrt.2025.109412.

Data availability

https://data.nist.gov/ (Data will be made available upon request and is available at)

References

[1] Nakajima H, Sugita T, Yokota T, Ishigaki T, Mogi Y, Araki N, et al. Characteristics and performance of the improved limb atmospheric spectrometer-II (ILAS-II) on board the ADEOS-II satellite. J Geophys Res Atmos 2006;111.

[2] Nowlan CR, McElroy CT, Drummond JR. Measurements of the - and -bands for determining temperature and pressure profiles from ACE–MAESTRO: forward model and retrieval algorithm. J Quant Spectrosc Radiat Transf 2007;108:371–88.

[3] Stevens MH, Englert CR, Harlander JM, England SL, Marr KD, Brown CM, et al. Retrieval of lower thermoscpheric temperatures from O_2 A band emission: the MIGHTI experiment on ICON. Space Sci Rev 2018;214.

[4] Stevens MH, Englert CR, Harlander JM, Marr KD, Harding BJ, Triplett CC, et al. Temperatures in the upper mesosphere and lower thermosphere from O2 atmospheric band emission observed by ICON/MIGHTI. Space Sci Rev 2022;218.

[5] Sun K, Yousefi M, Chan Miller C, Chance K, González Abad G, Gordon IE, et al. An optimal estimation-based retrieval of upper atmospheric oxygen airglow and temperature from SCIAMACHY limb observations. Atmos Meas Tech 2022;15:3721–45.

[6] Geddes A, Bösch H. Tropospheric aerosol profile information from high-resolution oxygen A-band measurements from space. Atmos Meas Tech 2015;8:859–74.

[7] Koelemeijer RBA, Stammes P, Hovenier JW, de Haan JF. A fast method for retrieval of cloud parameters using oxygen A band measurements from the Global Ozone Monitoring Experiment. J Geophys Res Atmos 2001;106:3475–90.

[8] Richardson M, McDuffie J, Stephens GL, Cronk HQ, Taylor TE. The OCO-2 oxygen A-band response to liquid marine cloud properties from CALIPSO and MODIS. J Geophys Res Atmos 2017;122:8255–75.

[9] Butz A, Guerlet S, Hasekamp O, Schepers D, Galli A, Aben I, et al. Toward accurate CO_2 and CH_4 observations from GOSAT. Geophys Res Lett 2011;38. n/a-n/a.

[10] Bovensmann H, Burrows JP, Buchwitz M, Frerick J, Noel S, Rozanov VV. SCIAMACHY: mission objectives and measurement modes. J Atmos Sci 1999;56:127–50.

[11] Veefkind JP, Aben I, McMullan K, Förster H, de Vries J, Otter G, et al. TROPOMI on the ESA Sentinel-5 Precursor: A GMES mission for global observations of the atmospheric composition for climate, air quality and ozone layer applications. Remote Sens Environ 2012;120:70–83.

[12] Eldering A, Taylor TE, O'Dell CW, Pavlick R. The OCO-3 mission: measurement objectives and expected performance based on 1 year of simulated data. Atmos Meas Tech 2019;12:2341–70.

[13] Crisp D, Atlas RM, Breon FM, Brown LR, Burrows JP, Ciais P, et al. The Orbiting Carbon Observatory (OCO) mission. Adv Space Res 2004;34:700–9.

[14] Miller CE, Crisp D, DeCola PL, Olsen SC, Randerson JT, Michalak AM, et al. Precision requirements for space-based data. J Geophys Res Atmos 2007;112.

[15] Miller CE, Brown LR, Toth RA, Benner DC, Devi VM. Spectroscopic challenges for high accuracy retrievals of atmospheric CO2 and the Orbiting Carbon Observatory (OCO) experiment. C R Phys 2005;6:876–87.

[16] Connor B, Bösch H, McDuffie J, Taylor T, Fu D, Frankenberg C, et al. Quantification of uncertainties in OCO-2 measurements of XCO2: simulations and linear error analysis. Atmos Meas Tech 2016;9:5227–38.

[17] Hobbs JM, Drouin BJ, Oyafuso F, Payne VH, Gunson MR, McDuffie J, et al. Spectroscopic uncertainty impacts on OCO-2/3 retrievals of XCO2. J Quant Spectrosc Radiat Transf 2020:257.

[18] Payne VH, Drouin BJ, Oyafuso F, Kuai L, Fisher BM, Sung K, et al. Absorption coefficient (ABSCO) tables for the Orbiting Carbon Observatories: version 5.1. J Quant Spectrosc Radiat Transf 2020:255.

[19] Drouin BJ, Benner DC, Brown LR, Cich MJ, Crawford TJ, Devi VM, et al. Multispectrum analysis of the oxygen A-band. J Quant Spectrosc Radiat Transf 2017;186:118–38.

[20] Long DA, Hodges JT. On spectroscopic models of the O2 A-band and their impact upon atmospheric retrievals. J Geophys Res Atmos 2012;117.

[21] Brown LR, Plymate C. Experimental line parameters of the oxygen A band at 760 nm. J Mol Spectrosc 2000;199:166–79.

[22] Robichaud DJ, Hodges JT, Brown LR, Lisak D, Masłowski P, Yeung LY, et al. Experimental intensity and lineshape parameters of the oxygen A-band using frequency-stabilized cavity ring-down spectroscopy. J Mol Spectrosc 2008;248:1–13.

[23] Predoi-Cross A, Hambrook K, Keller R, Povey C, Schofield I, Hurtmans D, et al. Spectroscopic lineshape study of the self-perturbed oxygen A-band. J Mol Spectrosc 2008;248:85–110.

[24] Ritter K, Wilkerson T. High-resolution spectroscopy of the oxygen A band. J Mol Spectrosc 1987;121:1–19.

[25] Schermaul R, Learner R. Precise line parameters and transition probability of the atmospheric A band of molecular O_2. JQSRT 1999;61:781–94.

[26] Yang S, Canagaratna MR, Witonsky SK, Coy SL, Steinfeld JI, Field RW, et al. Intensity measurements and collision-broadening coefficients for the oxygen A band measured by intracavity laser absorption spectroscopy. J Mol Spectrosc 2000;201:188–97.

[27] Xu S, Dai D, Xie J, Sha G, Zhang C. Quantitative measurements of O2 b ← X (2,1,0←0) bands by using cavity ring-down spectroscopy. Chem Phys Lett 1999;303:171–5.

[28] van Zee RD, Hodges JT, Looney JP. Pulsed, single-mode cavity ringdown spectroscopy. Appl Opt 1999;38:3951–60.

[29] Havey DK, Long DA, Okumura M, Miller C, Hodges J. Ultra-sensitive optical measurements of high-J transitions in the O 2 A-band. Chem Phys Lett 2009;483:49–54.

[30] Long DA, Havey DK, Okumura M, Miller CE, Hodges JT. O2 A-band line parameters to support atmospheric remote sensing. J Quant Spectrosc Radiat Transf 2010;111:2021–36.

[31] Watson JK. Rotational line intensities in 3Σ–1Σ electronic transitions. Can J Phys 1968;46:1637–43.

[32] Petrova TM, Solodov AM, Solodov AA, Deichuli VM, Fedorova AA. CO2-broadened lineshapes in the oxygen A-band. J Quant Spectrosc Radiat Transf 2024:314.

[33] Herman R, Wallis RF. Influence of vibration-rotation interaction on line intensities in vibration-rotation bands of diatomic molecules. J Chem Phys 1955;23:637–46.

[34] Rothman L, Gordon I, Babikov Y, Barbe A, Benner D, Bernath P. The HITRAN database: 2012 edition. J Quant Spectrosc Radiat Transfer 2013.

[35] Balasubramanian TK, Narayanan O. Magnetic dipole and electic quadrupole line strengths for the atmospheric oxygen ($b^1\Sigma^{+g}$ - $X^3\Sigma$ (g) system. Acta Phys Hung 1994;74:341–53.

[36] Rothman L, Gordon I, Babikov Y, Barbe A, Benner DC, Bernath P, et al. The HITRAN2012 molecular spectroscopic database. J Quant Spectrosc Radiat Transf 2013;130:4–50.

[37] Gordon I.E., Rothman L.S., Hill C., Kochanov R.V., Tan Y., Bernath P.F., et al. The HITRAN2016 molecular spectroscopic database. 2017;203:3–69.

[38] Karman T, Koenis MAJ, Banerjee A, Parker DH, Gordon IE, Van Der Avoird A, et al. O_2-O_2 and O_2-N_2 collision-induced absorption mechanisms unravelled. Nat Chem 2018;10:549–54.

[39] Gordon IE, Rothman LS, Hargreaves RJ, Hashemi R, Karlovets EV, Skinner FM, et al. The HITRAN2020 molecular spectroscopic database. J Quant Spectrosc Radiat Transf 2021.

[40] Adkins EM, Hodges JT. Assessment of the precision, bias and numerical correlation of fitted parameters obtained by multi-spectrum fits of the Hartmann-Tran line profile to simulated absorption spectra. J Quant Spectrosc Radiat Transf 2022:280.

[41] Reed ZD, Tran H, Ngo HN, Hartmann JM, Hodges JT. Effect of Non-Markovian collisions on measured integrated line shapes of CO. Phys Rev Lett 2023;130:143001.

[42] Tran H, Li G, Ngo NH, Ebert V. Pressure dependence of the measured line intensity and super-lorentzian effects in the absorption spectra of pure HCl. Phys Chem Chem Phys 2023;25:10343–52.

[43] Tran H, Li G, Ngo NH, Ebert V. Non-impact effects in the absorption spectra of HCl diluted in CO2, air, and He: measurements and predictions. J Chem Phys 2023:158.

[44] Fleisher AJ, Adkins EM, Reed ZD, Yi H, Long DA, Fleurbaey HM, et al. Twenty-five-fold reduction in measurement uncertainty for a molecular line intensity. Phys Rev Lett 2019;123:043001.

[45] Gamache RR, Goldman A, Rothman LS. Improved spectral parameters for the three most abundant isotopomers of the oxygen molecule. J Quant Spectrosc Radiat Transf 1998;59:495–509.

[46] Watson JK. Quadratic Herman-Wallis factors in the fundamental bands of linear molecules. J Mol Spectrosc 1987;125:428–41.

[47] Somogyi W, Yurchenko SN, Kim G-S. An ab inito spectroscopic model of the molecular oxygen atmospheric and infrared bands. Phys Chem Chem Phys 2024. Under Review.

[48] Babcock HD, Herxberg L. Fine structure of the red system of atmospheric oxygen bands. Astrophys J 1948;108:167–90.

[49] Yurchenko SN, Lodi L, Tennyson J, Stolyarov AV. Duo: A general program for calculating spectra of diatomic molecules. Comput Phys Commun 2016;202:262–75.

[50] Somogyi W, Yurchenko SN, Yachmenev A. Calculation of electric quadrupole linestrengths for diatomic molecules: application to the H(2), CO, HF, and O(2) molecules. J Chem Phys 2021;155:214303.

[51] Furtenbacher T, Horváth M, Koller D, Sólyom P, Balogh A, Balogh I, et al. MARVEL analysis of the measured high-resolution rovibronic spectra and definitive ideal-gas thermochemistry of the 16O2 molecule. J Phys Chem Ref Data 2019;48.

[52] Somogyi W, Yurchenko SN, Tennyson J. ExoMol line lists: empirical magnetic dipole and electric quadrupole spectra of the infrared bands of Oxygen (O_2). Mon Not R Astron Soc 2025. in preparation.

[53] Hodges JT, Layer HP, Miller WW, Scace GE. Frequency-stabilized single-mode cavity ring-down apparatus for high-resolution absorption spectroscopy. Rev Sci Instrum 2004;75:849–63.

[54] Long DA, Truong G-W, van Zee RD, Plusquellic DF, Hodges JT. Frequency-agile, rapid scanning spectroscopy: absorption sensitivity of 2×10^{-12} cm^{-1} $\mathrm{hz}^{-1/2}$ with a tunable diode laser. Appl Phys B 2014;114:489–95.

[55] Truong G-W, Douglass KO, Maxwell SE, van Zee RD, Plusquellic DF, Hodges JT, et al. Frequency-agile, rapid scanning spectroscopy. Nat Photonics 2013;7:532–4.

[56] Lin H, Reed Z, Sironneau V, Hodges J. Cavity ring-down spectrometer for high-fidelity molecular absorption measurements. J Quant Spectrosc Radiat Transf 2015;161:11–20.

[57] Hendricks JH, Olson DA. 1–15,000Pa absolute mode comparisons between the NIST ultrasonic interferometer manometers and non-rotating force-balanced piston gauges. Measurement 2010;43:664–74.

[58] Coursey J.S., Schwab, D.J., Tsai, J.J., and Dragoset, R.A. . Atomic weights and isotopic compositions (version 4.1). Gaithersburg, MD: National Institute of Standards and Technology; 2015.

[59] Tennyson J, Bernath PF, Campargue A, Császár AG, Daumont L, Gamache RR, et al. Recommended isolated-line profile for representing high-resolution spectroscopic transitions (IUPAC Technical Report). Pure Appl Chem 2014;86:1931–43.

[60] Adkins EM. Multi-spectrum analysis tool for spectroscopy (MATS). 2020. 10.18434/M32200.

[61] NIST Certificate of batch analysis. 107C2 2024.

[62] Cygan A, Lisak D, Trawiński R, Ciuryło R. Spectral line shape problem in the spectroscopic determination of the Boltzmann constant. In: Proceedings of the 20th International Conference on Spectral Line Shapes; 2010. p. 214–8.

[63] Tran H. Effect of incomplete collisions by classical molecular dynamics simulations. In: Hodges J.T., editor.2024.

[64] Gamache RR, Roller C, Lopes E, Gordon IE, Rothman LS, Polyansky OL, et al. Total internal partition sums for 166 isotopologues of 51 molecules important in planetary atmospheres: application to HITRAN2016 and beyond. J Quant Spectrosc Radiat Transf 2017;203:70–87.

[65] Joint Committee for Guides in Metrology. Evaluation of measurement data—Guide to the expression of uncertainty in measurement. JCGM 2008;100:1–116.

[66] Long DA, Reed ZD, Fleisher AJ, Mendonca J, Roche S, Hodges JT. High-accuracy near-infrared carbon dioxide intensity measurements to support remote sensing. Geophys Res Lett 2020;47:e2019GL086344.

[67] Fleurbaey H, Yi H, Adkins EM, Fleisher AJ, Hodges JT. Cavity ring-down spectroscopy of CO_2 near $\lambda = 2.06$ μm: accurate transition intensities for the Orbiting carbon observatory-2 (OCO-2) "strong band. J Quant Spectrosc Radiat Transf 2020;252:107104.